Regular Article

PHYSICAL CHEMISTRY RESEARCH
Published by the
Iranian Chemical Society
www.physchemres.org
info@physchemres.org

Phys. Chem. Res., Vol. 12, No. 1, 157-173, March 2024
DOI: 10.22036/pcr.2023.388675.2311

The Effect of Nonlinear Thermal Radiation on EMHD Casson Nanofluid over a Stretchable Riga Plate with Temperature-Dependent Viscosity and Chemical Reaction

I. El Glili* and M. Driouich

Laboratory of Research in Physics and Engineering Sciences (LRPSI), Polydisciplinary Faculty, Sultan Moulay Slimane University, Beni Mellal, 23000, Morocco

(Received 6 March 2023, Accepted 28 May 2023)

This study aimed to examine the flow of Electro-magnetohydrodynamic (EMHD) Casson nanofluid over a stretchable Riga plate with variable viscosity using and comparing two basic models called Reynolds' and Vogel's models. Brownian motion, thermophoresis, and nonlinear thermal radiation were considered. Using appropriate transformations, partial differential equations (PDEs) were converted into nonlinear ordinary differential equations (ODEs) and solved numerically using the Bvp4c method. The main goal was to visualize the effects of some parameters, such as the modified Hartmann number ($0.5 \leq E^* \leq 1.5$), the Casson fluid parameter ($0.3 \leq \beta \leq 1.1$), the dimensionless parameter ($0.5 \leq S \leq 1.5$), the suction parameter ($-0.5 \leq f_w \leq 0.5$), the Prandtl number ($1 \leq Pr \leq 10$), the radiation parameter ($1 \leq R_d \leq 5$), the space-dependent heat source ($0 \leq Q \leq 2$), the chemical reaction ($0.5 \leq \gamma_1 \leq 1.5$), the temperature-dependent heat source ($0 \leq Q^* \leq 2$), the Schmidt number ($1 \leq Sc \leq 1.8$), and the Brownian motion ($0.1 \leq Nb \leq 0.5$), on temperature and velocity profiles. The results revealed that the modified Hartmann number had a significant effect on velocity profiles, leading to the control of the flow. In addition, the increase in the radiation parameter led to an increase in the temperature.

Keywords: Variable viscosity, Non-Newtonian fluid, Heat source, Electro-magnetohydrodynamic, Bvp4c method

INTRODUCTION

Polymer solutions, suspensions, gels, and biological fluids are different types of fluids that represent a class of materials with complex flow behavior, departing from the linear relationship between shear stress and shear rate. These types of fluids are known as non-Newtonians. Many researchers have been attracted to non-Newtonian fluids due to their vast range of applications in manufacturing and engineering processes [1-4].

In 1959, Casson introduced a non-Newtonian model known as the Casson fluid model [5]. It is a shear-thinning liquid that exhibits a yield stress and is supposed to exhibit zero viscosity at an extremely high shear rate, a yield stress below which no flow occurs, and infinite viscosity at zero shear rate. The behavior of this model is similar to that of elastic solids, such as jelly, honey, fruit juices, soup, and blood, and has an important role in food technology, metal processing, and biological sciences. In the literature, numerous models have been suggested to describe the nature of non-Newtonian fluids. The effect of Coriolis force on the magnetohydrodynamics (MHD) micropolar two-phase dusty fluid across a stretched sheet was examined by Lou *et al.* [6]. They concluded that while the distribution of micro-rotation reduced with the increase in the volume concentration of dust particles, it increased with the increase in rotation and material parameters. Ali *et al.* [7] investigated the stationary 3D MHD rotating flow, comprising Maxwell and

*Corresponding author. E-mail: issa.elglilifpb@usms.ac.ma

tangent hyperbolic fluids, by passing a bi-directional stretching surface using the Cattaneo-Christov heat flux model. Considering the effects of the Lorentz force and radiation, Ali *et al.* [8] studied the mixed convection of micropolar fluid flow created by an inclined sheet. They noticed that increasing the inclination angle of the sheet resulted in the increased distribution of temperature within the micropolar fluid. Dufour and Soret effects on the MHD rotating flow of Oldroyd-B nanofluid across an extended sheet were examined by Ali *et al.* [9].

Nanotechnology involves the production and utilization of materials that are smaller than 100 nm in size. These materials are used extensively in various fields such as material science, agriculture, food production, cosmetics, medicine, and diagnostic procedures. As the size of materials decreases, their properties change at the atomic level. Nanoparticles have unique biological, optical, chemical, and physical properties that can be utilized for specific applications [10]. The technique of using a combination of base fluid and nanoparticles was first introduced by Choi [11]. The analysis of nanofluids has aroused the interest of researchers. Foukhari *et al.* [12], for instance, explored the shape effect of nanoparticles on heat transfer by free convection in the cylindrical cavity subjected to a heat flux. They found that heat transmission was done better with cylindrical nanoparticles than with spherical nanoparticles. Abderrahmane *et al.* [13] utilized the finite element method to perform the computational simulations of the MHD hybrid nanofluid with mixed convection within a 3D triangular porous cavity using a rotating cylinder and a zigzag wall. Ashraf *et al.* [14] performed bioconvection on the steady MHD tangent hyperbolic nanofluid passing through an elastic surface with variable thickness. They employed the Runge-Kutta technique to determine the differential equations and found that the power-law index (m) caused a decrease in the velocity distribution while the temperature showed the opposite behavior. Thermophoretic and radiation characteristics were found to greatly increase temperature distribution as Brownian motion enhanced. Recently, more studies have focused on the flow of nanofluids [15-21].

The motion of a fluid can undergo significant electrical conductivity when a strong external magnetic field is present. This phenomenon, referred to as flow control through MHD, has been studied under various conditions [22-26]. By applying a crossed electric and magnetic field, a wall-parallel Lorentz force was generated, which was the idea behind the Riga plate. The Riga plate is an electromagnetic actuator device that produces electric and magnetic fields used to control and direct fluid flow by the Lorentz force. It is an arrangement of electrodes and permanent magnets aligned perpendicular to each other and mounted on a flat surface. Shankaralingappa *et al.* [27] investigated the effect of the flow of thermophoretic particles with a Casson nanofluid based on sodium alginate on a nonlinear three-dimensional extending sheet. They reported that the increase in the thermophoretic parameter reduced the concentration profile and that the improvement in the Casson parameter was accompanied by an increase in the temperature and a decrease in the velocity. Ellahi *et al.* [28] examined the incompressible third-grade nanofluid flow using two classic models of viscosity. They used the Homotopy analysis method to solve the coupled nonlinear equation. Alotaibi and Rafique [29] numerically explored the effect of micro-rotation on the flow engendered by a Riga plate comprising a micropolar nanofluid. They considered the Brownian and thermophoresis effects using the Killer-box method. Hussain *et al.* [30] studied the effect of variable viscosity at the point of stagnation on the flow of Casson fluid over an extending/shrinking sheet with magnetic field and slip effects. They reported that while temperature decreased following the increase in the thermal parameter, it increased following an increase in the shrinking parameter. Khan *et al.* [31] studied the unsteady flow of magnetized Oldroyd-B fluid with a variable heat source and through a chemical reaction in a stretchable cylinder. Rafique *et al.* [32] considered the double stratification flow of micropolar nanofluid produced by a Riga plate that stretched exponentially using suction or injection and mixed convection. They observed that when the stratification of temperature increased, heat transfer at the surface declined but the mass transfer increased. Ramesh *et al.* [33] conducted a numerical study of the electro-magnetohydrodynamic (EMHD) flow of Maxwell nanofluids through a Riga plate with a temperature-dependent heat source/sink. The flow of Walters'-B fluid at the stagnation point across a Riga plate with Newtonian heating and thermal radiation was studied numerically by Shafiq *et al.* [34]. Ragupathi *et al.* [35] conducted a comparative study of Fe_3O_4 and Al_2O_3 nanoparticles on base liquids flows through a Riga plate with viscous dissipation.

Most of the aforementioned studies investigated the effect of thermal radiation using the Rosseland approximation, which is the emission of electromagnetic radiation in all directions by a heated substance. Since the flow temperature differences were very small, they described T^4 as a linear function of T. Bhatti *et al.* [36] investigated the effect of EMHD flow on viscous nanofluid with nonlinear thermal radiation through a Riga plate and found that whereas the radiation parameter increased the temperature profile, the EMHD tended to increase the velocity profile. Ganesh Kumar *et al.* [37] provided a numerical solution for the flow of magnetohydrodynamic Carreau nanofluid by considering the nonlinear thermal radiation and the slip effect. Eswaramoorthi *et al.* [38] examined the effect of the flow of Williamson fluid over a horizontal stretchable Riga plate in a porous medium using nonlinear thermal radiation and convective conditions. They found that as the thermal radiation increased, the heat transfer decreased.

The viscosity of a fluid is mainly influenced by its density, temperature, and nature. It is not accurate to assume that the viscosity is constant when the temperature is high; instead, the viscosity should be considered a temperature-dependent variable. The calculation of flow parameters will lead to significant errors if the temperature-dependent viscosity is not taken into account. The effect of variable permeability and viscosity on the Blasius flow of Carreau nanofluid on a Riga plate was investigated by Hakeem *et al.* [39]. They used Vogel's model to describe the variation in the viscosity. Their findings showed that the retardation of the fluid was caused by the viscosity parameter. Fatunmbi and Adeosun [40] studied the exponentially varying viscosity of the flow of Eyring-Powell nanofluid by considering the higher-order chemical reaction, nonlinear radiation, Darcy-Forchheimer flow, and viscous dissipation on a vertical Riga plate in a porous medium. Tabassum *et al.* [41] used the modified Brinkman number with hybrid carbon nanotube nanofluids to study the effect of temperature-dependent viscosity on the flow over a moving or fixed Riga plate.

The comprehensive review of the literature presented above highlights the lack of attention paid to the effect of nonlinear thermal radiation on the EMHD flow of the Casson nanofluid with temperature-dependent viscosity. None of the previously mentioned studies specifically addressed this problem. Therefore, the novelty of the present research is to explore the influence of temperature-dependent viscosity in the above-mentioned context. Reynolds' and Vogel's models were compared taking into consideration the effect of thermophoresis and Brownian motion, nonlinear thermal radiation, and non-uniform heat source. The differential partial equations (PDEs) were converted into ordinary differential equations (ODEs) using suitable transformation. The equations were numerically solved using the Bvp4c method. The findings were examined graphically to determine the effect of different physical factors on velocity, temperature, and concentration.

MATHEMATICAL FORMULATION

In this study, the 2D laminar, steady, and incompressible flows of Casson nanofluid over a stretchable Riga plate were investigated. The viscosity of the nanofluid was assumed to be variable. Two equal but opposite forces were applied parallel to the stretching axis to keep the origin fixed. The velocity at the stretching surface was $u = u_s = bx$ while the velocity at a distance away from the surface was $u_\infty = ax$. T_f and T_∞ were considered as the temperature on the surface and the ambient temperature, respectively, as shown in Fig. 1 where a and b are positive constants with dimensions (s^{-1}). The nanofluid model was developed using the effects of both Brownian motion and thermophoresis.

The rheological model for the Casson fluid, as described in [30], is presented below:

$$\tau = -pI + \mu_B \left(1 + \frac{1}{\beta}\right) \delta_1 \tag{1}$$

Under the above assumption and supposing that the nanoparticle was dilute, the governing equations were formulated as in [42-43]:

$$\frac{\partial u}{\partial x} + \frac{\partial v}{\partial y} = 0 \tag{2}$$

$$u\frac{\partial u}{\partial x} + v\frac{\partial u}{\partial y} = u_\infty \frac{\partial u_\infty}{\partial x} + \frac{1}{\rho}\frac{\partial}{\partial y}\left(\mu_B \left(1 + \frac{1}{\beta}\right)\left(\frac{\partial u}{\partial y}\right)\right) - \frac{\pi J_0 m_0}{8\rho} \exp\left(\frac{-\pi}{l} y\right) \tag{3}$$

$$u\frac{\partial T}{\partial x} + v\frac{\partial T}{\partial y} = \alpha_f \frac{\partial^2 T}{\partial y^2} + \psi\left[D_B \frac{\partial C}{\partial y}\frac{\partial T}{\partial y} + \frac{D_T}{T_\infty}\left(\frac{\partial T}{\partial y}\right)^2\right] - \frac{1}{\rho C_p}\frac{\partial q_r}{\partial y} + \frac{q'''}{\rho C_p} \tag{4}$$

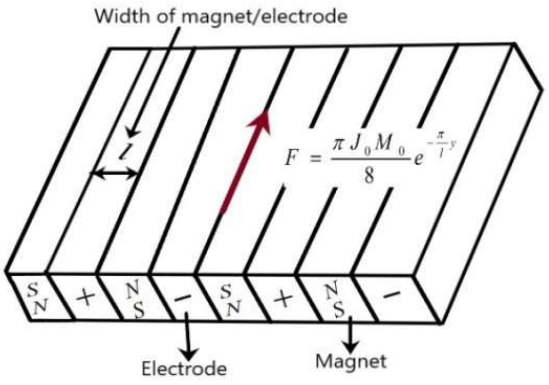

(a)

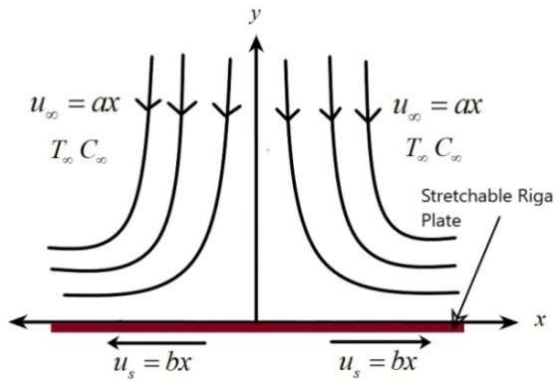

(b)

Fig. 1. a) Structure of the Riga plate; b) Physical configuration of the flow.

$$u\frac{\partial C}{\partial x} + v\frac{\partial C}{\partial y} = D_B\frac{\partial^2 C}{\partial y^2} + \frac{D_T}{T_\infty}\left(\frac{\partial T}{\partial y}\right)^2 - K_r^2(C - C_\infty)\left(\frac{T}{T_\infty}\right)^n \exp\left(\frac{-E_0}{\delta T}\right) \quad (5)$$

The boundary conditions were as follows:

$$u = ax\,; v = v_w\,; -K\frac{\partial T}{\partial y} = h_f\left(T_f - T\right)\,; C = C_w \quad at\ y = 0$$
$$u \to u_\infty\,; T \to T_\infty\,; C \to C_\infty \quad as\ y \to \infty \quad (6)$$

where q_r is the nonlinear thermal radiation and q''' is the non-uniform heat source/sink, as expressed in [44-45] and shown below:

$$q_r = -\frac{4\sigma^*}{3k^*}\frac{\partial T^4}{\partial y} = -\frac{16\sigma^*}{3k^*}T^3\frac{\partial T}{\partial y} \quad (7)$$

$$q''' = \frac{kU_s}{xv_f}\left[Q\left(T_f - T_\infty\right)e^{-\eta} + Q^*(T - T_\infty)\right] \quad (8)$$

Simplification of Mathematical Formulation

By introducing the following quantities into Eq. (3) to (5),

$$u = axf'(\eta)\ ;\ v = -\sqrt{av_f}f(\eta)\ ;\ \mu_B = \frac{\overline{\mu}_B}{\mu_B^*}\ ;$$
$$T = \left(T_f - T_\infty\right)\theta(\eta) + T_\infty\ ;$$

$$C = \left(C_f - C_\infty\right)\Phi(\eta) + C_\infty\ ;\ \eta = \sqrt{\frac{a}{v_f}}y\ ;$$
$$u = \frac{\partial \psi}{\partial y}\ ;\ v = -\frac{\partial \psi}{\partial x} \quad (9)$$

Eq. (3), (4) and (5) was developed as follows:

$$A\left(\frac{\partial \mu_B}{\partial \eta}\right)\left(1 + \frac{1}{\beta}\right)f'' + A\mu_B\left(1 + \frac{1}{\beta}\right)f''' - f'^2 + ff'' + E^*\exp(-S\eta) + 1 = 0 \quad (10)$$

$$\left[1 + \frac{4}{3}R_d\left((\theta_r - 1)\theta + 1\right)^3\right]\theta'' + Pr\left[f\theta' + N_b\theta'\phi' + N_t\theta'^2\right] + 4R_d\theta'^2\left((\theta_r - 1)\theta + 1\right)^2(\theta_r - 1) + Qf' + Q^*\theta = 0 \quad (11)$$

$$\phi'' + S_c f\phi' + \frac{N_t}{N_b}\theta'' - S_c\gamma_1\left((\theta_r - 1)\theta + 1\right)^n \exp\left(-\frac{E}{(\theta_r - 1)\theta + 1}\right)\phi = 0 \quad (12)$$

where

$$A = \frac{\mu_B}{\rho v_f}\ ;\ E^* = \frac{\pi J_0 m_0 x}{8\rho u_\infty^2}\ ;\ S = \frac{\pi}{l}\sqrt{\frac{v_f}{a}}\ ;$$
$$E = \frac{E_0}{\delta T_\infty}\ ;\ R_d = \frac{16\sigma^* T_\infty^3}{3k^* k_f}\ ;\ \theta_r = \frac{T_f}{T_\infty}\ ;$$
$$Pr = \frac{\mu_f C_p}{k}\ ; N_b = \frac{\tau D_B(C_w - C_\infty)}{v_f}\ ;$$
$$N_t = \frac{\tau D_T(T_w - T_\infty)}{T_\infty v_f}\ ; Sc = \frac{v_f}{D_B}\ ;\ \gamma_1 = \frac{K_r^2}{a} \quad (13)$$

in which the conditions at the boundary were as follows:

$$\begin{cases} f'(0) = 0, \quad f(0) = f_w, \quad \theta'(0) = -Bi[1-\theta(0)], \\ \phi(0) = 1 \\ f'(\infty) \to \lambda, \ \theta(\infty) \to 0, \quad \phi(\infty) \to 0. \end{cases} \tag{14}$$

Furthermore, it should be noted that the parameter E^* was dependent on x rather than having a fixed value. Under these circumstances, we examined the availability of local similarity solutions, which, in turn, could be used to determine how the parameter E^* was affected at a specific location above the plate.

Case 1: Reynolds Model

The variable viscosity was considered as [30]:

$$\mu_B = e^{-P\theta} \tag{15}$$

using the Maclaurin series, Eq. (15) can be rewritten as follows:

$$\mu_B = 1 - P\theta \tag{16}$$

or

$$\frac{\partial \mu_B}{\partial \eta} = -P\frac{\partial \theta}{\partial \eta} \tag{17}$$

Equation (10) can be written as:

$$-AP\theta'\left(1+\tfrac{1}{\beta}\right)f'' + A(1-P\theta)\left(1+\tfrac{1}{\beta}\right)f''' - f'^2 + ff'' + E^*\exp(-S\eta) + 1 = 0 \tag{18}$$

Case 2: Vogel's Model

In this case, the viscosity was calculated as follows [30]:

$$\mu_B = \frac{C}{C^*}\left(1 - \frac{\theta S}{B^2}\right) \tag{19}$$

$$\frac{\partial \mu_B}{\partial \eta} = -\frac{CS}{C^*B^2}\frac{\partial \theta}{\partial \eta} \tag{20}$$

Accordingly, Eq. (10) can be rewritten as:

$$-A\frac{CS}{C^*B^2}\theta'\left(1+\frac{1}{\beta}\right)f'' + A\frac{C}{C^*}\left(1-\frac{\theta S}{B^2}\right)\left(1+\frac{1}{\beta}\right)f''' - f'^2 + ff'' + E^*\exp(-S\eta) + 1 = 0 \tag{21}$$

Physical Quantities

The skin friction coefficient, Nusselt number, and Sherwood number are the physical parameters of interest that influence the flow. Skin friction coefficient is a dimensionless quantity that quantifies the frictional force between the fluid at the boundary and the wall surface. Furthermore, Nusselt and Sherwood numbers exhibit the rate of heat and mass transfer between the fluid and the upper surface of the plate, respectively. Mathematical expressions for the shear stress, local heat flux (q_w), skin friction coefficient (Cf_x), and the local Nusselt number (Nu_x) can be written as follows, respectively:

$$\begin{aligned} \tau_w &= \mu_B\left(1+\frac{1}{\beta}\right)\left(\frac{\partial u}{\partial y}\right)_{y=0} \quad ; \\ q_w &= (q_r)_{y=0} - k_f\left(\frac{\partial T}{\partial y}\right)_{y=0} \quad ; \\ q_m &= -D_B\left(\frac{\partial C}{\partial y}\right)_{y=0} \end{aligned} \tag{22}$$

$$\begin{aligned} C_{fx} &= \frac{\tau_w}{\frac{1}{2}\rho u_s^2} \quad ; \quad Nu_x = \frac{xq_w}{k_f\left(T_f - T_\infty\right)} \quad ; \\ Sh_x &= \frac{xq_m}{D_B\left(C_f - C_\infty\right)} \end{aligned} \tag{23}$$

Non-dimensional equations of the above equations are presented below:

$$\begin{aligned} \frac{1}{2}Re_x^{1/2}C_{fx} &= \mu_B\left(1+\frac{1}{\beta}\right)f''(0) \quad ; \\ Re_x^{-1/2}Sh_x &= -\phi(0)\,; \\ Re_x^{-1/2}Nu_x &= -\theta'(0)\left[1+\tfrac{4}{3}Rd(\theta(0)(\theta_r-1)+1)^3\right] \end{aligned} \tag{24}$$

NUMERICAL METHODS

Numerical Procedure

The corresponding PDEs were rewritten as a system of non-linear ODEs, Eqs. (11), (12), (18), (21), and (14), with the last one reflecting the conditions at the boundary, utilizing suitable transformation and then solved using the Bvp4c method. The code was based on the three-stage Lobatto IIIa formula and used finite difference methods, which require the conversion of the equations to a system of first-order ODEs.

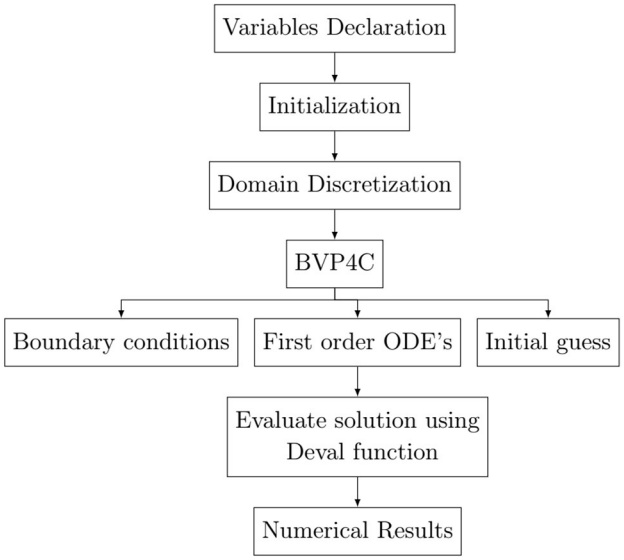

Fig. 2. The procedure of the numerical solution.

Other researchers have extensively employed this solver to find a solution for the boundary value problem. In this study, the value $\eta = \eta_\infty = 10$ was used since for $\eta > 10$, the results did not show a significant difference. Thus, [0, 10] was used as the domain of the problem instead of [0, ∞[. The procedure is indicated in Fig. 2.

Code Validation

A comparison of our findings with those reported in [46-48]concerning $f''(0)$ with the absence of $E^* = 0$, $f_w = 0$, $\beta \to \infty$, and constant viscosity, with replacing the values of $f'(0) = \alpha$, is presented in Table 1. As can be seen in Table 1, our model showed quite excellent accuracy when our findings were compared with those available in the literature. Tables 2 and 3 validate the results of the present study in comparison with those reported in [49] and [50] for $\theta'(0)$ and $\phi'(0)$ in a special case with $E^* = -1$, S = 0, Pr = Sc = 10, and $Bi \to \infty$. An excellent correlation was found between the values.

Table 1. A Comparison of the Outcome for $f''(0)$ When $E^* = f_w = 0$ and $\beta \to \infty$

α	[46]	[47]	[48]	Present
0.0	1.23258	1.23258	1.23258	1.232587
0.1	1.14656	1.14656	1.14656	1.146560
0.2	1.05113	1.05113	1.05113	1.051129
0.5	0.71330	0.71329	0.71329	0.713295
1.0	0.00000	0.00000	0.00000	0.000000
2.0	-1.8873	-1.8873	-1.8873	-1.88730
5.0	-10.264	-10.264	-10.264	-10.2647

Table 2. A comparison of $\theta'(0)$ When $E^* = -1$, $S = 0$, $Pr = Sc = 10$, and $Bi \to \infty$

N_b	N_t	[49]	[50]	Present
0.1	0.1	0.9524	0.9523	0.9522
0.1	0.3	0.5201	0.5200	0.5201
0.1	0.5	0.3211	0.3210	0.3211
0.3	0.1	0.2522	0.2521	0.2521
0.3	0.3	0.1355	0.1354	0.1355
0.3	0.5	0.0833	0.0832	0.0833
0.5	0.1	0.0543	0.0542	0.0542
0.5	0.3	0.0291	0.0291	0.0291
0.5	0.5	0.0179	0.0179	0.0179

Table 3. A Comparison of $\phi'(0)$ When $E^* = -1, S = 0, Pr = Sc = 10,$ and $Bi \to \infty$

N_b	N_t	[49]	[50]	Present
0.1	0.1	2.1294	2.1294	2.12935
0.1	0.3	2.5286	2.5286	2.52854
0.1	0.5	3.0351	3.0351	3.03497
0.3	0.1	2.4100	2.4100	2.40999
0.3	0.3	2.6088	2.6088	2.60877
0.3	0.5	2.7519	2.7519	2.75181
0.5	0.1	2.3836	2.3835	2.38354
0.5	0.3	2.4984	2.4984	2.49833
0.5	0.5	2.5731	2.5731	2.57305

RESULTS AND DISCUSSION

In this study, the quantitative effects of various flow parameters, such as modified Hartmann number (E^*), Casson parameter (β), dimensionless parameter (S), chemical reaction parameter (γ_1), suction parameter (f_w), on velocity, temperature, and concentration were examined. Figures 3-18 illustrate the results for both viscosity models, *i.e.*, Reynolds' and Vogel's models. The values of fixed parameters for graphical results, Nusselt number, Sherwood number, and skin friction coefficient were chosen as follows: $E^* = 0.5$, $\beta = 0.5$, $f_w = 0.2$, $S = 0.5$, $\lambda = 1$, $Bi = 1$, $Rd = 5$, $\theta r = 1.3$, $Pr = 6.8$, $Q = 0.1$, $Q^* = 0.1$, $Nb = 0.1$, $Nt = 0.1$, $Sc = 1.0$, $\gamma_1 = 0.3$.

Velocity Profiles

Figures 3-4 were plotted to illustrate the behavior of temperature-dependent viscosity in Reynolds' model (P) and Vogel's model (C). It was observed that the viscosity factor in Reynolds' model tended to increase the velocity profile due to the reduction of the shear in the momentum boundary layer. The opposite trend was observed for the viscosity factor in Vogel's model due to the fact that the viscous force was stronger than the inertial force. Therefore, the fluid friction restricted the movement of the fluid.

The change in the velocity profile against the modified Hartmann number is depicted in Fig. 5. As it can be seen in Fig. 5, the velocity profile increased following an increase in the modified Hartmann number. This phenomenon can be attributed to the fact that the Lorentz force created by the

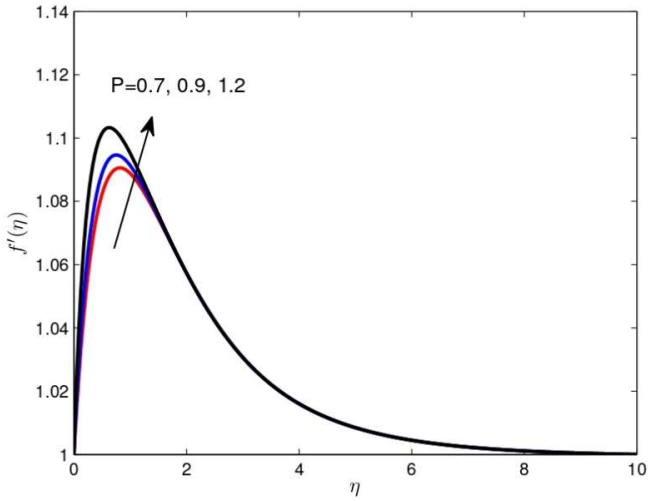

Fig. 3. The effect of velocity factor in Reynolds' model (P).

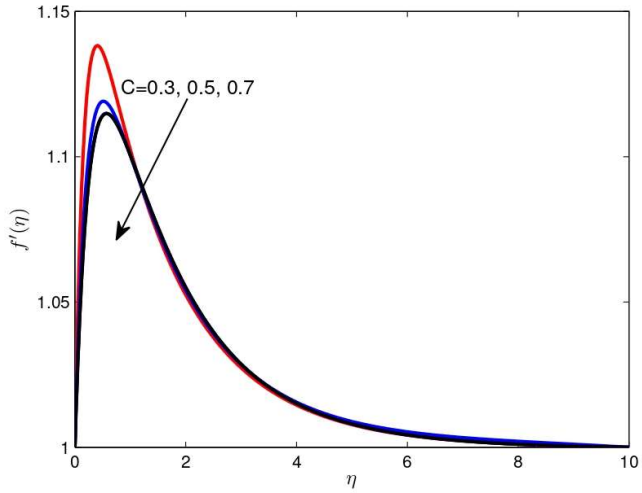

Fig. 4. The effect of velocity factor in Vogel's model (C).

Riga plate was reduced due to the enhancement of the electric field, which acted as an accelerating force and reduced the frictional resistance.

Figure 6 was plotted to show the effect of the Casson fluid parameter on the velocity profile. It was found that β tended to enhance the velocity. This effect can be explained by the substantial decrease in the yield strength associated with higher β values. As the yield strength decreased, the fluid flew more easily. It should be noted that the fluid became Newtonian as $\beta \rightarrow \infty$.

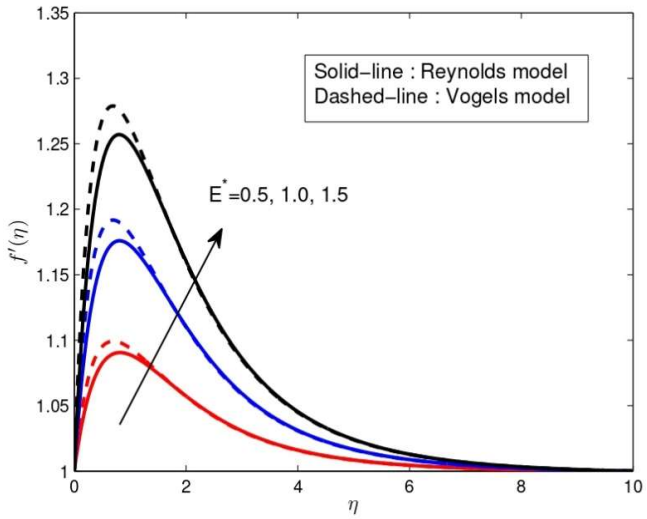

Fig. 5. The effect of E^* on the velocity profile.

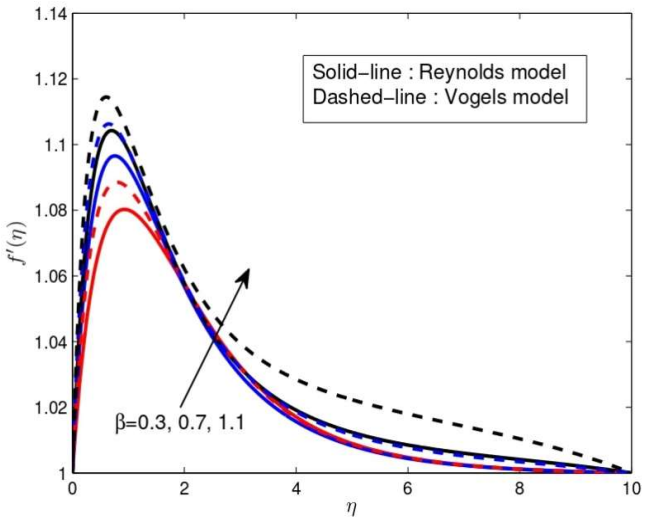

Fig. 6. The effect of the Casson parameter (β) on the velocity profile.

Figure 7 shows the effect of the dimensionless parameter (S) on the velocity profile. As can be seen in Fig. 7, the increase in parameter S led to a reduction in the width of the momentum boundary layer, which diminished the velocity profile. Figures 1-7 demonstrate that Vogel's model provided better results compared with Reynolds' model.

Figure 8 shows that the velocity of the fluid decelerated due to the increase in the suction parameter. This reduction could have been caused by the attraction of fluid toward the boundary due to strong suction, which, in turn, could have increased the viscosity. Therefore, it can be stated that the shear stress reduction took place at low velocity in the boundary layer.

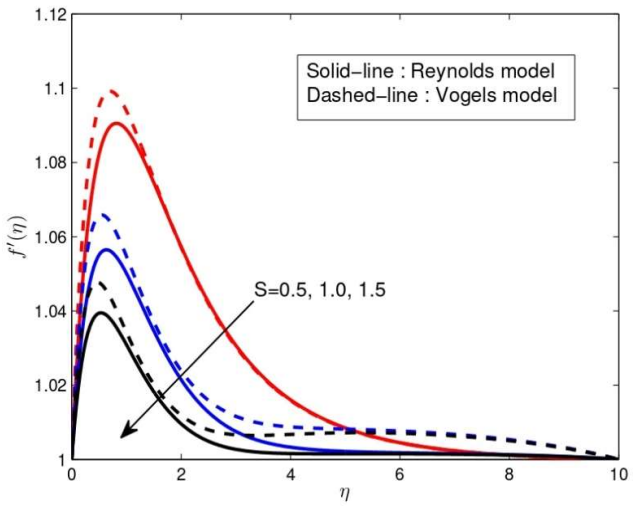

Fig. 7. The effect of the dimensionless parameter (S) on the velocity profile.

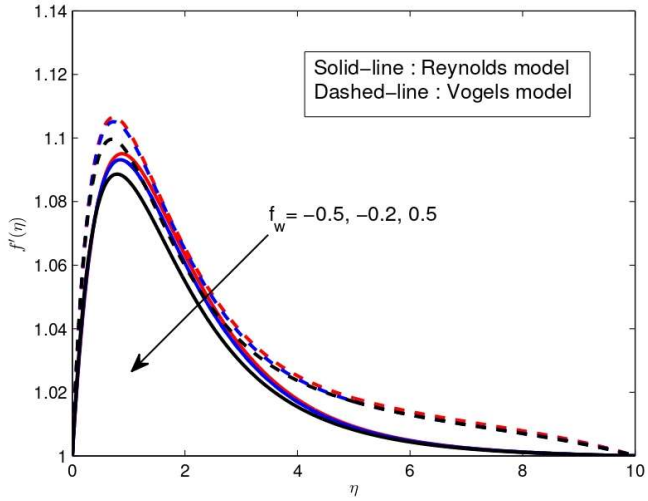

Fig. 8. The effect of the suction parameter (f_w) on the velocity profile.

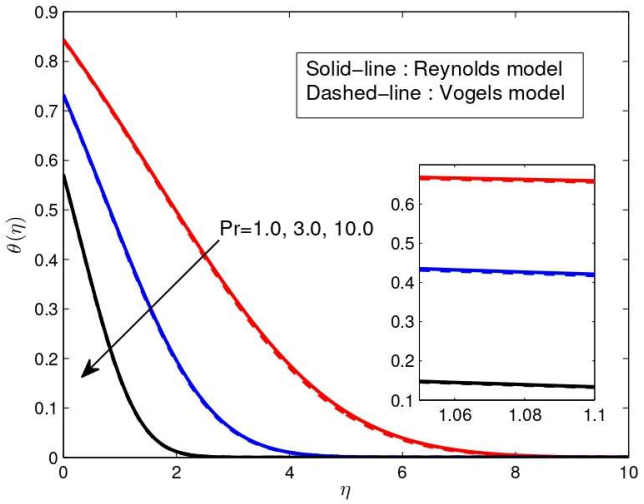

Fig. 9. Temperature distribution for the changes in the Prandtl number (Pr).

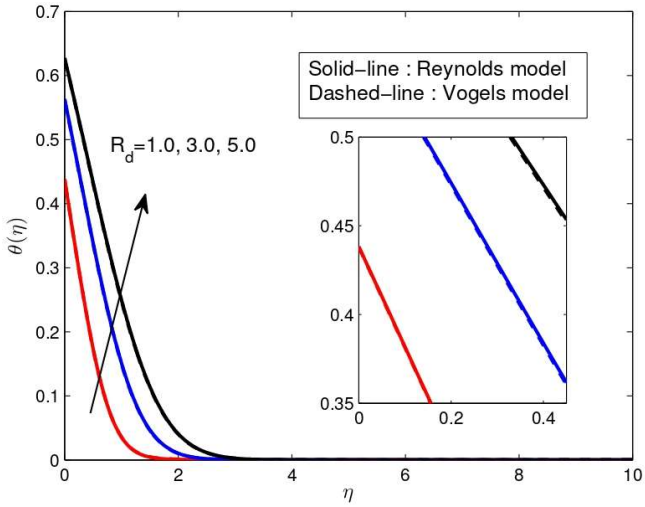

Fig. 10. Temperature distribution for the changes in the radiation parameter (R_d).

Temperature Profiles

The temperature distribution for different Prandtl numbers is plotted in Fig. 9. In fact, the Prandtl number was the rate of momentum diffusivity to thermal diffusivity. for higher Prandtl numbers, the thermal diffusivity became smaller, causing a decrease in the boundary layer thickness, which, in turn, reduced the temperature.

The temperature distribution for different values of radiation parameter (R_d) is shown in Fig. 10. It was observed that temperature increased with an increase in the R_d. Since the radiation parameter was the ratio of conductive heat transfer to radiative heat transfer, the increase in the conduction effect inside the thermal boundary layer due to the increase in R_d increased the temperature. The results agree qualitatively with those reported in the literature [51]. This result can be helpful in utilizing the thermal radiation mechanism to regulate the ratio of heat transfer characteristics.

Figure 11 captures the effect of the heating parameter (θ_r) on temperature distribution. Figure 11 reveals that the temperature rose with an increase in θ_r. This could be due to the increase in the thermal boundary layer, which improved the production of internal heat, resulting in the facilitation of heat transfer and an increase in the temperature field.

The change in the temperature against the Biot number is depicted in Fig. 12, which shows that the increase in the Biot

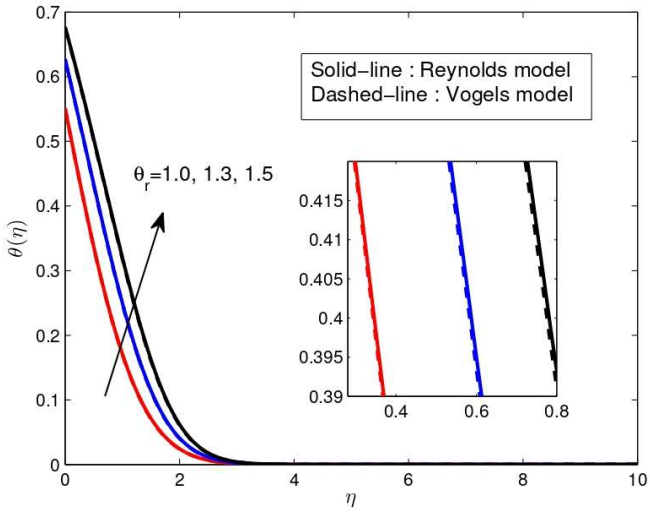

Fig. 11. Temperature distribution following the changes in the heating parameter (θ_r).

number resulted in an increase in the temperature distribution due to increased thermal boundary layer thickness caused by the heat transfer through convection at the surface, which, in turn, caused the fluid to heat up. The graphs showing the effect of Biot number on concentration and velocity profiles are not presented here since the effect was almost negligible.

Figures 13-14 illustrate space-dependent (Q) and temperature-dependent parameters (Q^*) for the effect of heat

generation/absorption on temperature distribution. It can be observed that the increasing Q and Q^* led to an increase in the temperature distribution due to the heat generated in the fluid, making the thermal boundary layer thicker.

Concentration Profiles

Figure 15 was plotted to show the effect of the chemical reaction parameter (γ_1) on the concentration profile. It is evident from Fig. 15 that an increase in γ_1 decreased the concentration due to the increase in the number of solute molecules, which, in turn, reduced the solute boundary layer thickness.

As can be seen in Fig. 16, an increase in the Brownian motion (Nb) resulted in a decrease in the concentration profile. In fact, irregular motion and stronger mixing of the fluid were both caused by an increase in the Brownian motion of the particles.

An opposite behavior is captured in Fig. 17. That is, an increase in the thermophoresis parameter (Nt) enhanced the concentration profile. The particles were more likely to move

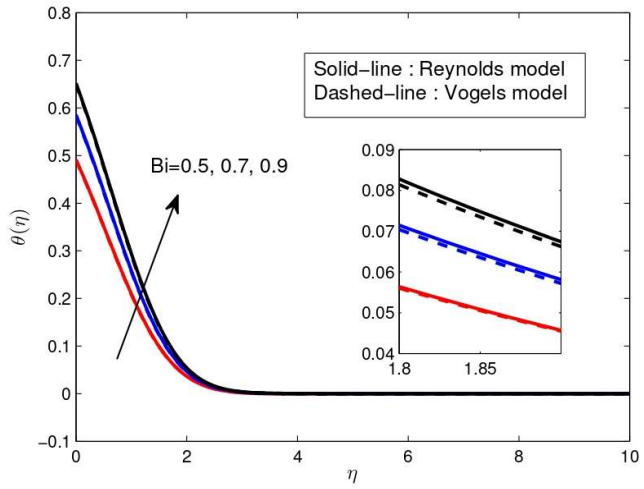

Fig. 12. Temperature distribution following the changes in the Biot number (Bi).

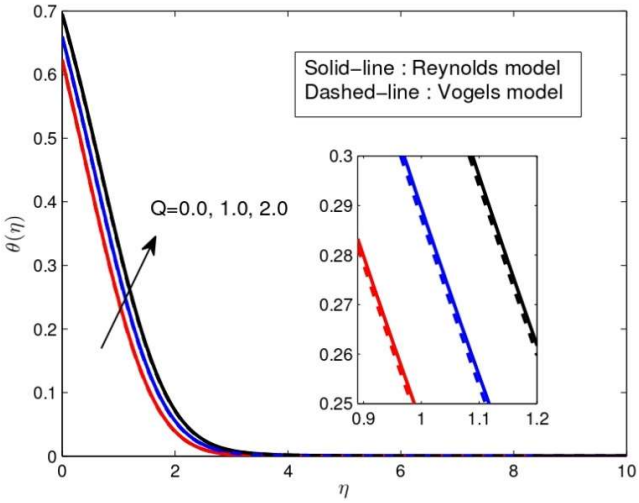

Fig. 13. Temperature distribution following changes in the space-dependent heat source (Q).

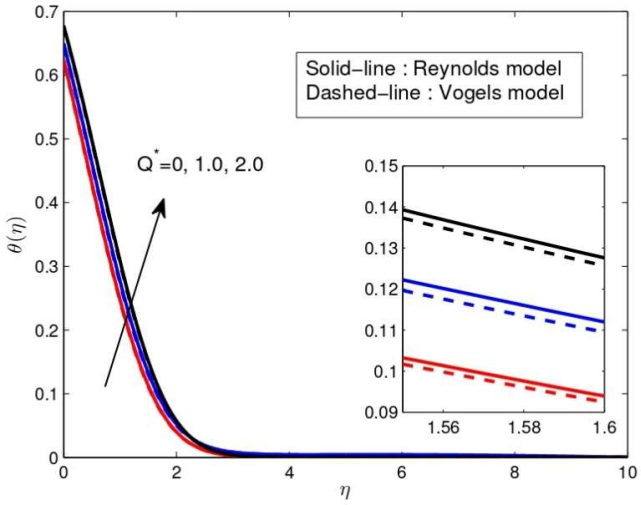

Fig. 14. Temperature distribution following the changes in the temperature-dependent heat source (Q^*).

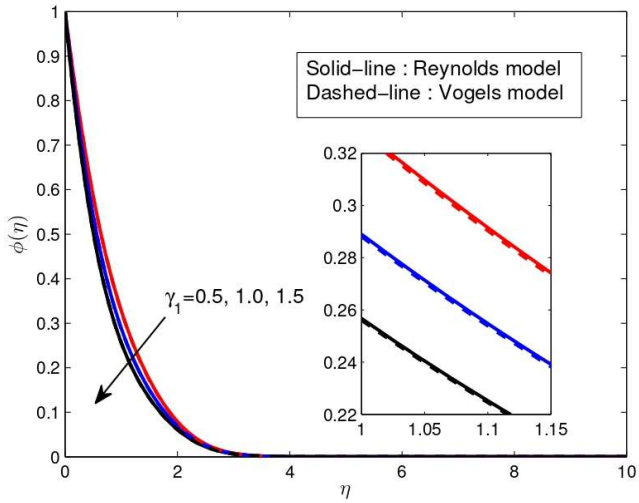

Fig. 15. The effect of chemical reaction (γ_1) on the concentration profile.

toward the regions with higher to lower temperatures, which, in turn, led to some changes in the concentration profile.

The effect of the Schmidt number on the concentration profile is illustrated in Fig. 18. Based on Fig. 18, the concentration profile diminished when the Schmidt number increased. The Schmidt number was defined as the rate between the momentum diffusivity and mass diffusivity, meaning that higher Schmidt numbers were expected to correlate with lower mass diffusion.

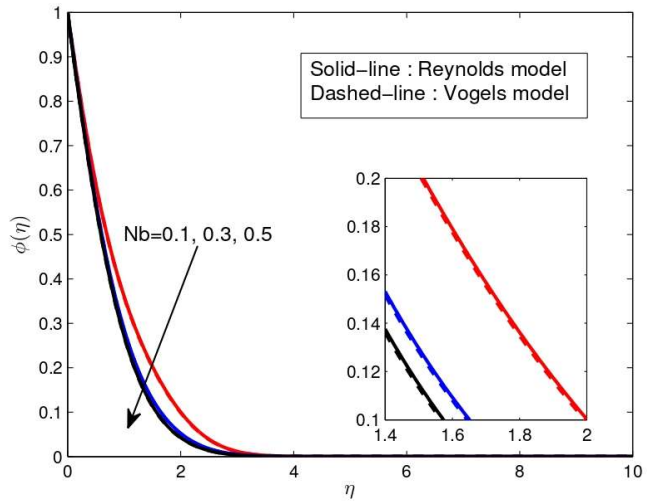

Fig. 16. The effect of the Brownian motion (Nb) on the concentration profile.

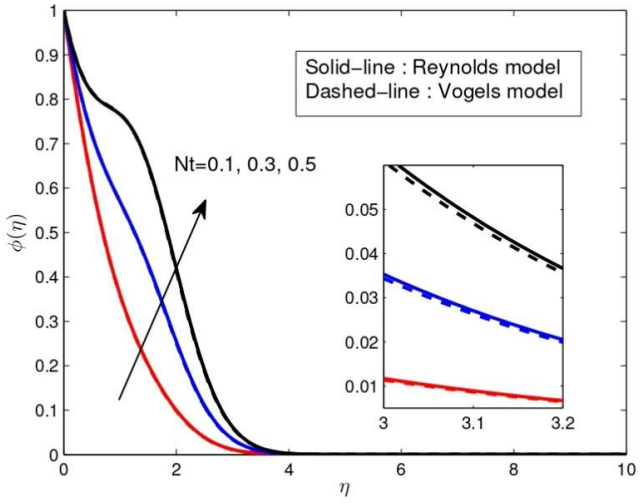

Fig. 17. The effect of thermophoresis parameter (Nt) on the concentration profile.

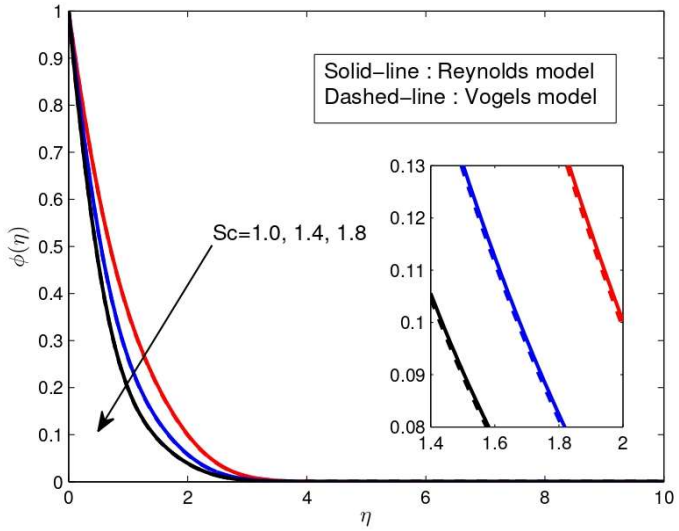

Fig. 18. The effect of Schmidt number (Sc) on the concentration profile.

To summarize, it can be stated that the thermal behavior of the fluid differed in Vogel's model compared to Reynolds' model. Based on the data, the decrease in the fluid temperature was prevalent in the flow domain. This implies that Vogel's model provided a faster rate of heat transfer and consequently resulted in a higher level of cooling efficiency than did Reynolds' model.

Table 4 shows the effect of the Schmidt number, the chemical reaction, the Brownian motion, and the thermophoresis parameter on the Sherwood number for both Reynolds' and Vogel's models. It is evident from Table 4 that the Sherwood number increased with an increase in the Schmidt number, chemical reaction, and Brownian motion. The rate of increase in the Sherwood number was 59.18%, 8.35%, and 1.92% for the Reynolds' model and 59.21%, 8.32%, and 1.95% for the Vogel's model for the Schmidt number, chemical reaction, and Brownian motion, respectively. However, an opposite effect was observed for the thermophoresis parameter. That is, the Sherwood number decreased with a rate of 31% for Reynolds' model and 31.21% for Vogel's model when the thermophoresis parameter increased.

Table 5 shows the Nusselt numbers for both Reynolds' and Vogel's models. The Nusselt number, which is a measure of convective heat transfer in a fluid near a solid boundary,

Table 4. The Sherwood Number (Sh_x) for Vogel's and Reynolds' Models

				Sh_x	
Sc	γ_1	*Nb*	*Nt*	Vogel's model	Reynolds' model
1.0	0.3	0.1	0.1	0.924207	0.921739
2.0				1.471498	1.467269
3.0				1.913947	1.908565
1.0	0.9	0.1	0.1	1.135235	1.133344
	1.2			1.229702	1.228020
1.0	0.3	0.3	0.1	1.021263	1.018066
		0.5		1.041228	1.037710
1.0	0.3	0.1	0.3	0.680721	0.679822
			0.5	0.468257	0.469018

Table 5. The Nusselt Number (Nu_x) for Vogel's and Reynolds' Models

				Nu_x	
Pr	R_d	*Q*	Q^*	Vogel's model	Reynolds model
1.0	1.0	0.0	0.0	0.854007	0.851842
2.0				1.053096	1.051127
3.0				1.170133	1.168440
1.0	3.0	0.0	0.0	1.413175	1.408928
	5.0			1.843892	1.838415
1.0	1.0	1.0	0.0	0.475491	0.470849
		2.0		0.085250	0.075055
1.0	1.0	0.0	1.0	0.238856	0.221567
			1.2	-0.007509	-0.099540

Table 6. The Skin Friction Coefficient (Cf_x) for Vogel's and Reynolds' Models

				Cf_x	
E^*	β	*S*	*fw*	Vogel's model	Reynolds model
0.1	0.5	0.5	0.2	0.002036	0.106314
0.5				0.009929	0.526817
1.0				0.019310	1.042752
0.1	1.5	0.5	0.2	0.001658	0.087244
	2.0			0.001597	0.084171
0.1	0.5	1.0	0.2	0.001597	0.081471
		1.5		0.001328	0.066628
0.1	0.5	0.5	0.4	0.002040	0.112495
			0.6	0.002041	0.118519

increased following the increase in the radiation parameter and Prandtl number. Table 5 shows that Vogel's model gave higher values than did Reynolds' model, meaning that the increase in heat transfer was greater in Vogel's model. The rate of increase in the Nusselt number in Reynolds' model was 23.39% and 30.48%, respectively, while it was 23.31% and 30.47% in Vogel's model, respectively. On the other hand, the Nusselt number decreased as did the space-dependent and temperature-dependent heat source parameters. The reduction rate of the local Nusselt number in Reynolds' model was about 84.05% and 144.92%, respectively, while it was 82.07% and 103.17% in Vogel's model, respectively. In Vogel's model, a significant improvement was observed in cooling efficiency.

The effect of the modified Hartmann number, Casson parameter, dimensionless parameter (S), and suction parameter on skin coefficient friction is shown in Table 6. It can be observed that the shear stress rose with an increase in the value of the modified Hartmann number and suction parameter. The increase in the rate of skin friction coefficient in Reynolds' model was 395.52% and 5.35%, respectively, while it was 387.67% and 0.05% in Vogel's model, respectively. An opposite behavior was observed for the Casson and dimensionless (S) parameters, with a reduction rate of 3.52% and 18.22% in Reynolds' model and 3.68% and 16.84% in Vogel's model, respectively.

CONCLUSIONS

The objective of this study was to investigate the effect of variable viscosity on EMHD Casson nanofluid with nonlinear thermal radiation and non-uniform heat source over a stretchable Riga plate. Velocity, temperature, and concentration profiles for two classic models of viscosity, namely, Reynolds' and Vogel's models, were determined to evaluate the effects of various physical factors. Using a similarity transformation, the PDEs were converted into ODEs and solved numerically using the Bvp4c method. The results were provided in graphical and tabular forms, and the following conclusions were reached:

- While increasing the Casson parameter and modified Hartmann number enhanced the velocity, increasing the suction and dimensionless parameters decreased velocity;
- The temperature increased when radiation, space-dependent, and temperature-dependent parameters for the heat source were increased. The opposite trend was observed for the Prandtl number;
- The concentration parameter increased and decreased following an increase in the thermophoresis parameter and Brownian motion, respectively;
- Concerning the Nusselt number, Vogel's model showed better results than did Reynolds' model.

NOMENCLATURE

a, b	Constants
Bi	Biot number
C_∞	Ambient fluid concentration
C_f	Surface concentration
C_p	Specific heat (J K^{-1})
D_T	Diffusion coefficient
D_B	Brownian diffusion
E	Activation energy parameter
E^*	Modified Hartmann number
f_w	Suction parameter
$f'(y)$	Dimensionless normal velocity
J_0	Current density
k_f	Thermal conductivity (W m^{-1} K^{-1})
Kr	Chemical reaction rate
k^*	Mean absorption coefficient (m^{-1})
m_0	Magnetization of magnets (Tesla)
n	Fitted rate constant
Nt	Thermophoresis parameter
Nb	Brownian motion
q_r	Radiative heat flux (W m^{-2})
Pr	Prandtl number
Q	Space-dependent heat source
Q^*	Temperature-dependent heat source
Re	Reynolds number
S	Associated with magnets and electrodes
Sc	Schmidt number
R_d	Radiation parameter
T_f	Surface temperature (K)
T_∞	Ambient temperature (K)
u, v	Velocity in x, y direction (m s^{-1})
u_∞	Velocity at the free stream (m s^{-1})
us	Velocity at the sheet (m s^{-1})

Greek Symbols

α_f	Thermal diffusivity ($m^2 s^{-1}$)
β	Casson fluid parameter
γ_1	Chemical reaction
θr	Heating parameter
μ_B	Plastic dynamic viscosity (pa s)
μ	Dynamic viscosity (pa s)
σ^*	Stefan Boltzmann constant ($W m^{-2} K^{-4}$)
ν	Kinematic viscosity ($m^2 s^{-1}$)
τ	Shear stress
θ	Dimensionless temperature
ρ	Density ($kg\ m^{-3}$)
θ_w	Heating parameter

REFERENCES

[1] Salahuddin, T.; Malik, M. Y.; Hussain, A.; Awais, M.; Bilal, S., Mixed Convection Boundary Layer Flow of Williamson Fluid with Slip Conditions over a Stretching Cylinder by Using Keller Box Method. *Int. J. Nonlinear Sci. Numer. Simul*. **2017**, *18* (1), 9-17, DOI: 10.1515/ijnsns-2015-0090.

[2] Roy, N. C.; Pop, I., Flow and heat transfer of a second-grade hybrid nanofluid over a permeable stretching/shrinking sheet. *Eur. Phys. J. Plus*. **2020**, *135* (9), 1-19, DOI: 10.1140/epjp/s13360-020-00788-9.

[3] Ahmad, A., Flow control of non-newtonain fluid using riga plate: Reiner-Phillipoff and Powell-Eyring viscosity models. *J. Appl. Fluid Mech.* **2019**, *12* (1), 127-133, DOI:10.29252/jafm.75.253.28897.

[4] Ahmed, S. E.; Hussein, A. K.; Mansour, M. A.; Raizah, Z. A.; Zhang, X., Mhd Mixed Convection in Trapezoidal Enclosures Filled With Micropolar Nanofluids. *Nanosci. Technol. An Int. J.* **2018**, *9*, 343-372, DOI:10.1615/nanoscitechnolintj.2018026118.

[5] Ramesh, G. K.; Prasannakumara, B. C.; Gireesha, B. J.; Rashidi, M. M., Casson fluid flow near the stagnation point over a stretching sheet with variable thickness and radiation. *J. Appl. Fluid Mech.* **2016**, *9* (3), 1115-1022, DOI: 10.18869/acadpub.jafm.68.228.24584.

[6] Lou, Q.; Ali, B.; Rehman, S. U.; Habib, D.; Abdal, S.; Shah, N. A.; Chung, J. D., Micropolar Dusty Fluid: Coriolis Force Effects on Dynamics of MHD Rotating Fluid When Lorentz Force Is Significant. *Math*. **2022**, *10*, 1-13, DOI: 10.3390/math10152630.

[7] Ali, B.; Thumma, T.; Habib, D.; salamat, N.; Riaz, S., Finite element analysis on transient MHD 3D rotating flow of Maxwell and tangent hyperbolic nanofluid past a bidirectional stretching sheet with Cattaneo Christov heat flux model, *Therm. Sci. Eng. Prog.* **2022**, *28*, 101089, DOI: 10.1016/j.tsep.2021.101089.

[8] Ali, B.; Shafiq, A.; Siddique, I.; Al-Mdallal, Q.; Jarad, F., Significance of suction/injection, gravity modulation, thermal radiation, and magnetohydrodynamic on dynamics of micropolar fluid subject to an inclined sheet via finite element approach, *Case Stud. Therm. Eng*. **2021**, *28*, 101537, DOI: 10.1016/j.csite.2021.101537.

[9] Ali, B.; Hussain, S.; Nie, Y.; Hussein, A. K.; Habib, D., Finite element investigation of Dufour and Soret impacts on MHD rotating flow of Oldroyd-B nanofluid over a stretching sheet with double diffusion Cattaneo Christov heat flux model, *Powder Technol*. **2021**, *377*, 439-452, DOI: 10.1016/j.powtec.2020.09.008.

[10] Ahmed, A.; Nadeem, S., The study of (Cu, TiO_2, Al2O3) nanoparticles as antimicrobials of blood flow through diseased arteries. *J. Mol. Liq*. **2016**, *216*, 615-623, DOI: 10.1016/j.molliq.2016.01.059.

[11] Choi, S. U. S., Enhancing thermal conductivity of fluids with nanoparticles. *Am. Soc. Mech. Eng. Fluids Eng. Div. FED.* **1995**, *231*, 99-105.

[12] Foukhari, Y.; Sammouda, M.; Driouich, M.; Belhouideg, S., Nanoparticles Shape Effect on Heat Transfer by Natural Convection of Nanofluid in a Vertical Porous Cylindrical Enclosure Subjected to a Heat Flux. *Recent Advances in Fuzzy Sets Theory, Fractional Calculus, Dynamic Systems and Optimization*, Springer International Publishing, **2023**, DOI: 10.1007/978-3-031-12416-7_37.

[13] Abderrahmane, A.; Qasem, N. A. A.; Younis, O.; Marzouki, R.; Mourad, A.; Shah, N. A.; Chung, J. D., MHD Hybrid Nanofluid Mixed Convection Heat Transfer and Entropy Generation in a 3-D Triangular Porous Cavity with Zigzag Wall and Rotating Cylinder, *Math*. **2022**, *10*, DOI:10.3390/math10050769.

[14] Ashraf, M. Z.; Rehman, S. U.; Farid, S.; Hussein, A. K.; Ali, B.; Shah, N. A.; Weera, W., Insight into Significance of Bioconvection on MHD Tangent Hyperbolic Nanofluid Flow of Irregular Thickness across a Slender Elastic Surface, *Math*. **2022**, *10*, 1-17,

DOI: 10.3390/math10152592.

[15] Biswal, U.; Chakraverty, S.; Ojha, B. K.; Hussein, A. K., Numerical investigation on nanofluid flow between two inclined stretchable walls by Optimal Homotopy Analysis Method, *J. Comput. Sci*. **2022**, *63*, 101759, DOI: 10.1016/j.jocs.2022.101759.

[16] Ali, B.; Siddique, I.; Ahmadian, A.; Senu, N.; Ali, L.; Haider, A., Significance of Lorentz and Coriolis forces on dynamics of water based silver tiny particles via finite element simulation, *Ain Shams Eng. J*. **2022**, *13*, 101572, DOI: 10.1016/j.asej.2021.08.014.

[17] Wakif, A.; Shah, N. A., Hydrothermal and mass impacts of azimuthal and transverse components of Lorentz forces on reacting Von Kármán nanofluid flows considering zero mass flux and convective heating conditions, *Waves in Random and Complex Media*. **2022**, DOI: 10.1080/17455030.2022.2136413.

[18] Ali, B.; Siddique, I.; Ahmad, H.; Askar, S., Influence of nanoparticles aggregation and Lorentz force on the dynamics of water-titanium dioxide nanoparticles on a rotating surface using finite element simulation, *Sci. Rep.* **2023**, *13*, 4702, DOI: 10.1038/s41598-023-31771-w.

[19] Zhang, B.; Tang, L.; Zhang, H.; Ali, B.; Shah, N. A.; Jeon, Y., Finite element study of nanoparticles spacing and radius on dynamics of water fluid subject to microgravity environment, *Results Phys*. **2023**, *47*, 106355, DOI: 10.1016/j.rinp.2023.106355.

[20] Ali, B.; Shafiq, A.; Alanazi, M. M.; Hendi, A. A.; Hussein, A. K.; Shah, N. A., Significance of Nanoparticle Radius and Gravity Modulation on Dynamics of Nanofluid over Stretched Surface via Finite Element Simulation: The Case of Water-Based Copper Nanoparticles, *Math*. **2023**, *11*, 1-15, DOI:10.3390/math11051266.

[21] Ali, F. H.; Hamzah, H. K.; Hussein, A. K.; Jabbar, M. Y.; Talebizadehsardari, P., MHD mixed convection due to a rotating circular cylinder in a trapezoidal enclosure filled with a nanofluid saturated with a porous media, *Int. J. Mech. Sci*. **2020**, *181*, DOI: 10.1016/j.ijmecsci.2020.105688.

[22] Bhuvaneswari, M.; Eswaramoorthi, S.; Sivasankaran, S.; Hussein, A. K., Cross-diffusion effects on MHD mixed convection over a stretching surface in a porous medium with chemical reaction and convective condition, *Eng. Trans*. **2019**, *67*, 3-19, DOI: 10.24423/EngTrans.820.20190308.

[23] Mansour, M. A.; Rashad, A. M.; Mallikarjuna, B.; Hussein, A. K.; Aichouni, M.; Kolsi, L., MHD mixed bioconvection in a square porous cavity filled by gyrotactic microorganisms, *Int. J. Heat Technol*. **2019**, *37*, 433-445, DOI: 10.18280/ijht.370209.

[24] Ahmed, S. E.; Hussein, A. K.; Mohammed, H. A.; Adegun, I. K.; Zhang, X.; Kolsi, L.; Hasanpour, A.; Sivasankaran, S., Viscous dissipation and radiation effects on MHD natural convection in a square enclosure filled with a porous medium, *Nucl. Eng. Des*. **2014**, *266*, 34-42, DOI: 10.1016/j.nucengdes.2013.10.016.

[25] Hussein, A. K.; Ashorynejad, H. R.; Sivasankaran, S.; Kolsi, L.; Shikholeslami, M.; Adegun, I. K., Modeling of MHD natural convection in a square enclosure having an adiabatic square shaped body using Lattice Boltzmann Method, *Alexandria Eng. J*. **2016**, *55*, 203-214, DOI: 10.1016/j.aej.2015.12.005.

[26] Shah, N. A.; Ebaid, A.; Oreyeni, T.; Yook, S. J., MHD and porous effects on free convection flow of viscous fluid between vertical parallel plates: advance thermal analysis, *Waves in Random and Complex Media*. **2023**, DOI: 10.1080/17455030.2023.2186717.

[27] Shankaralingappa, B. M.; Madhukesh, J. K.; Sarris, I. E.; Gireesha, B. J.; Prasannakumara, B. C., Influence of thermophoretic particle deposition on the 3D flow of sodium alginate-based casson nanofluid over a stretching sheet. *Microm.* **2021**, *12* (12), 1474, DOI: 10.3390/mi12121474.

[28] Ellahi, R.; Raza, M.; Vafai, K., Series solutions of non-Newtonian nanofluids with Reynolds' model and Vogel's model by means of the homotopy analysis method. *Math. Comput. Model.* **2012**, *55* (7-8), 1876-1891, DOI: 10.1016/j.mcm.2011.11.043.

[29] Alotaibi, H.; Rafique, K., Numerical analysis of micro-rotation effect on nanofluid flow for vertical riga plate. *Cryst.* **2021**, *11* (11), 1315, DOI: 10.3390/cryst11111315.

[30] Hussain, A.; Afzal, S.; Rizwana, R.; Malik, M. Y., MHD stagnation point flow of a Casson fluid with variable viscosity flowing past an extending/shrinking

sheet with slip effects. *Phys. A Stat. Mech. Its Appl.* **2020**, *553*, 124080, DOI: 10.1016/j.physa.2019.124080.

[31] Khan, M.; Yasir, M.; Alshomrani, A. S.; Sivasankaran, S.; Aladwani, Y. R.; Ahmed, A., Variable heat source in stagnation-point unsteady flow of magnetized Oldroyd-B fluid with cubic autocatalysis chemical reaction. *Ain Shams Eng. J.* **2022**, *13* (3), 101610, DOI: 10.1016/j.asej.2021.10.005.

[32] Rafique, K.; Alotaibi, H.; Ibrar, N.; Khan, I., Stratified Flow of Micropolar Nanofluid over Riga Plate: Numerical Analysis. *Ener*. **2022**, *15* (1), 316, DOI: 10.3390/en15010316.

[33] Ramesh, G. K.; Roopa, G. S.; Gireesha, B. J.; Shehzad, S. A.; Abbasi, F. M., An electro-magneto-hydrodynamic flow Maxwell nanoliquid past a Riga plate: a numerical study. *J. Brazilian Soc. Mech. Sci. Eng.* **2017**, *39* (11), 4547-4554, DOI: 10.1007/s40430-017-0900-z.

[34] Shafiq, A.; Hammouch, Z.; Turab, A., Impact of radiation in a stagnation point flow of Walters' B fluid towards a Riga plate. *Therm. Sci. Eng. Prog.* **2018**, *6*, 27-33, DOI: 10.1016/j.tsep.2017.11.005.

[35] Hakeem, A.K.; Ragupathi, P.; Ganga, B.; Nadeem, S., Three-dimensional viscous dissipative flow of nanofluids over a riga plate. *J. Heat Mass Transf. Res.* **2021**, *8* (1), 49-60, DOI: 10.22075/JHMTR.2020.21120.1300.

[36] Bhatti, M. M.; Abbas, T.; Rashidi, M. M., Effects of thermal radiation and electromagnetohydrodynamics on viscous nanofluid through a Riga plate. *Multidiscip. Model. Mater. Struct.* **2016**, *12* (4), 605-618, DOI: 10.1108/MMMS-07-2016-0029.

[37] Kumar, G. K.; Ramesh, G. K.; Gireesha, B. J.; Rashad, A. M., On stretched magnetic flow of Carreau nanofluid with slip effects and nonlinear thermal radiation. *Nonlinear Eng.* **2019**, *8* (1), 340-349, DOI: 10.1515/nleng-2017-0120.

[38] Eswaramoorthi, S.; Loganathan, K.; Faisal, M.; Botmart, T.; Shah, N. A., Analytical and numerical investigation of Darcy-Forchheimer flow of a nonlinear-radiative non-Newtonian fluid over a Riga plate with entropy optimization, *Ain Shams Eng. J.* **2023**, *14*, 101887, DOI: 10.1016/j.asej.2022.101887.

[39] Abdul Hakeem, A. K.; Nayak, M. K.; Makinde, O. D., Effect of exponentially variable viscosity and permeability on blasius flow of Carreau Nano Fluid over an electromagnetic plate through a porous medium, *J. Appl. Comput. Mech*. **2019**, 5, 390-401, DOI: 10.22055/jacm.2018.26307.1322.

[40] Fatunmbi, E. O.; Adeosun, A. T., Nonlinear radiative Eyring-Powell nanofluid flow along a vertical Riga plate with exponential varying viscosity and chemical reaction, Int. Commun. *Heat Mass Transf.* **2020**, *119*, 104913, DOI: 10.1016/j.icheatmasstransfer.2020.104913.

[41] Tabassum, R.; Al-Zubaidi, A.; Rana, S.; Mehmood, R.; Saleem, S., Slanting transport of hybrid (MWCNTs-SWCNTs/H_2O) nanofluid upon a Riga plate with temperature dependent viscosity and thermal jump condition, *Int. Commun. Heat Mass Transf*. **2022**, *135*, 106165, DOI: 10.1016/j.icheatmasstransfer.2022.106165.

[42] Asogwa, K. K.; Goud, B. S.; Reddy, Y. D.; Ibe, A. A., Suction effect on the dynamics of EMHD casson nanofluid over an induced stagnation point flow of stretchable electromagnetic plate with radiation and chemical reaction. *Results Eng.* **2022**, *15*, 100518, DOI: 10.1016/j.rineng.2022.100518.

[43] Vaidya, H. K.; Prasad, V.; Vajravelu, K.; Wakif, A.; Basha, N. Z.; Manjunatha, G.; Vishwanatha, U. B., Effects of variable fluid properties on oblique stagnation point flow of a casson nanofluid with convective boundary conditions. *Defect Diffus. Forum.* **2020**, *401*, 183-196, DOI: 10.4028/www.scientific.net/DDF.401.183.

[44] Mabood, F.; Fatunmbi, E. O.; Benos, L.; Sarris, I. E., Entropy Generation in the Magnetohydrodynamic Jeffrey Nanofluid Flow Over a Stretching Sheet with Wide Range of Engineering Application Parameters. *Int. J. Appl. Comput. Math.* **2022**, *8* (3), 1-18, DOI: 10.1007/s40819-022-01301-9.

[45] Mallikarjuna, B.; Rashad, A. M.; Hussein, A. K.; Hariprasad Raju, S., Transpiration and Thermophoresis Effects on Non-Darcy Convective Flow Past a Rotating Cone with Thermal Radiation, *Arab. J. Sci. Eng*. **2016**, *41*, 4691-4700, DOI:10.1007/s13369-016-2252-x.

[46] Wang, C. Y., Stagnation flow towards a shrinking sheet. *Int. J. Non. Linear. Mech.* **2008**, *43* (5), 377-382, DOI: 10.1016/j.ijnonlinmec.2007.12.021.

[47] Nandy, S. K.; Pop, I., Effects of magnetic field and thermal radiation on stagnation flow and heat transfer of nanofluid over a shrinking surface. *Int. Commun. Heat Mass Transf.* **2014**, *53*, 50-55, DOI: 10.1016/j.icheatmasstransfer.2014.02.010.

[48] Lok, Y. Y.; Ishak, A.; Pop, I., MHD stagnation-point flow towards a shrinking sheet. *Int. J. Numer. Methods Heat Fluid Flow.* **2011**, *21* (1), 61-72, DOI: 10.1108/09615531111095076.

[49] Khan, W. A.; Pop, I., Boundary-layer flow of a nanofluid past a stretching sheet. *Int. J. Heat Mass Transf.* **2010**, *53* (11-12), 2477-2483, DOI: 10.1016/j.ijheatmasstransfer.2010.01.032.

[50] Dalir, N.; Dehsara, M.; Nourazar, S.S., Entropy analysis for magnetohydrodynamic flow and heat transfer of a Jeffrey nanofluid over a stretching sheet. *Ener.* **2015**, *79*, 351-362, DOI: 10.1016/j.energy.2014.11.021.

[51] Pal, D.; Mondal, S.; Mondal, H., Entropy generation on MHD Jeffrey nanofluid over a stretching sheet with nonlinear thermal radiation using spectral quasilinearisation method. *Int. J. Ambient Ener.* **2021**, *42* (15), 1712-1726, DOI: 10.1080/01430750.2019.1614984.